Profiling Float Measurements of the Recirculation Gyre South of the Kuroshio Extension in May–November, 2004

Shuiming Chen,[1] Bo Qiu, and Peter Hacker

Department of Oceanography

University of Hawaii at Manoa

Honolulu, Hawaii

Journal of Geophysical Research

December 29, 2006

[1] *Corresponding author address:* Dr. Shuiming Chen, Department of Oceanography, University of Hawaii at Manoa, 1000 Pope Road, Honolulu, HI 96822. E-mail: schen@soest.hawaii.edu

Abstract

During May–November, 2004, 20 profiling floats were deployed in the recirculation gyre (RG) region south of the Kuroshio Extension (KE). With the KE and RG being in a stable state, most of these floats remained within the RG, resulting in a large number of satellite position fixes for estimating the velocities at the parking depth (1,500 db), and of T/S (Temperature/Salinity) profiles for estimating the geostrophic velocities above the parking depth. The flows of the RG at different depths in the upper 1,500 db are found to be approximately parallel to each other, with the speed at the surface (35 cm s^{-1}) being about three and a half times larger than that at the parking depth (10 cm s^{-1}). By analyzing the full-depth CTD (Conductivity-Temperature-Depth) profiles in the RG, in addition to the velocity estimates, we found that the vertical structure of the RG velocity field was dominated by the barotropic and first baroclinic modes. The two modes are combined in such a way that the resulting RG circulates anticyclonically in the same direction from the surface to the bottom and has an anticyclonic bottom velocity on the order of 5 cm s^{-1}. From the barotropic component (depth-averaged) of the RG velocity field, the RG transport with one standard error is estimated at $101\pm8 \times 10^6 m^3\ s^{-1}$.

1 Introduction

After separating from the coast of Japan near 35°N, the Kuroshio Extension (hereafter, KE) flows eastward with two quasi-stationary meanders before reaching the Shatsky Rise (Fig. 1). Over this segment, the eastward transport of the KE is augmented by the presence of the southern recirculation gyre (hereafter RG) (e.g. Wijffels et al. 1998). In climatological surface dynamic height maps such as those shown in Fig. 1, the RG is identifiable by closed contours south of the KE. The existence of the RG can also be seen from the synthesis of available direct velocity data for near-surface drifters from 1989-2001 (Niiler et al. 2003). Because the KE and RG interact dynamically, a better understanding of the RG helps us to understand the KE system and the KE's role in the general circulation and climate of the North Pacific.

Direct velocity measurements of the RG were first made in 1981-1982 using a moored current meter array along 152°E from 28°N to 41°N (Schmitz et al. 1982; Niiler et al. 1985). Unlike the climatology in Fig. 1, the velocity measurements in the upper (i.e., 500 m) portion and near the bottom showed that every 2-3 months there was an eddy passing by the array south of the KE (Schmitz et al. 1982). The deployment and retrieval hydrographic surveys (Fig. 2 in Niiler et al. 1985) showed that south of the KE in July 1980 and June 1982 there existed cyclonic eddies, and that in May 1981 the region was occupied by a less energetic eddy field; no clear RG was seen in those surveys.

The RG offshore to southeast Japan was measured by a full-depth CTD/LADCP (Lowered Acoustic Current Doppler Profiler) section as a part of the World Ocean Circulation Experiment (WOCE) P10 cruise in November 1993 (Firing 1998); the station locations are indicated by the LADCP depth-averaged velocity vectors in Fig. 1. In the present study, the depth-averaged velocity from a full depth profile will be referred to as the barotropic component, in the same sense as the barotropic dynamical mode. As shown by the vectors in Fig. 1, the RG had a barotropic component of 5-10 cm s^{-1}. The presence of the RG is clearly indicated by the broad

southwestward flow from 34°N to the southern end of the section at 32.7°N (Fig. 2). Within the RG, the observed southwestward flow is highly barotropic and its volume transport is estimated at about 86 Sv (Sv = 10^6 m^3 s^{-1}) .

The RG was more recently observed by the full-depth LADCP along 152°30′E in July 2000 and along 146°25′E in May 2001; both of these sections reached as far south as 30°N (Yoshikawa et al. 2004). The westward transports south of the KE were 34 Sv and 50 Sv along 152°30′E and 146°25′E, respectively. By using the concurrent satellite altimetric data, Yoshikawa et al. showed that during both of their surveys, the KE had a convoluted path with large-amplitude eddies on its two sides. Yoshikawa et al. also found that both the KE and the southern RG had bottom currents as strong as 10 cm s^{-1}, in agreement with the WOCE result shown in Fig. 2.

The different behaviors of the RG in the *in situ* measurements can be understood in terms of the temporal variations of the KE system found from satellite altimetry data over the past decade. By analyzing the altimetric sea surface height (SSH) since 1992, Qiu and Chen (2005) showed that the KE and its RG in the past decade oscillated between two dynamic states. Before 1995 and after 2002, the KE was in a stable sate (i.e., it was strong and remained at an approximately constant latitude between 35-36°N) and the RG was well represented by a single positive SSH maximum. During the period from 1996–2001, the KE path underwent large meridional excursions and there existed only weak SSH maxima south of the KE. The transition between the two dynamic states is instigated by the westward-propagating long Rossby waves, which in turn are induced by surface wind forcing in the Northeast Pacific (Qiu and Chen 2005). In terms of the bimodal states of the RG, the WOCE LADCP measurement in 1993 was made when the RG was in the stable state, and the LADCP measurements by Yoshikawa et al. (2004) in 2000 and 2001 were made when the RG was in the unstable state. The moored current meter measurements in 1981-1982 (Schmitz et al. 1982) appear to have been made when the RG was in the unstable state (i.e., when the KE was in a weakened state; see Fig. 11 in Qiu 2003).

While the surface characteristics of the RG have recently been examined in detail owing to the

accumulation of the surface drifter and satellite altimetry measurements (Niiler et al. 2003; Qiu 2003), information about the vertical structure of the RG remains fragmentary. The objective of the present study seeks to clarify the RG's vertical structure by using profiling float and full-depth CTD data from the Kuroshio Extension System Study (KESS) program, during the period from May–November 2004 when the KE/RG was in the stable state. Owing to the largely stationary nature of the RG during the analysis period, the floats sampled the area repeatedly, reducing uncertainty in the analysis. A representative vertical structure of the stable-state RG and an estimate of its transport are obtained.

2 Data

As a part of the KESS collaborative research project, 20 Apex profiling floats were deployed in 2004: four at the end of April, and sixteen in June (see Fig. 3 for their deployment locations and http://www.soest.hawaii.edu/snol/ for up-to-date float trajectories and T/S profiles). After the initial deployment, each float remained at the sea surface until six hours after the instrument's start-time, then dove to its preset parking depth (1,500 db). 107 hours following the dive time, the float began its ascent towards the surface, which took about 4.5 hours. It remained at the sea surface until 13 hours had elapsed since the beginning of its ascent, then dove again. A complete cycle from one dive to the next dive is thus 120 hours (5 days). Each float measured temperature and salinity at its parking depth, and at 72 specified pressures as it rose; the pressure intervals are 100 db at pressures greater than 1,000 db, 30 db between 400–1,000 db, 10 db between 100–400 db, and 5 db between 5–100 db. While the float was at the sea surface, it transmitted T/S data messages to the ARGOS satellites every 44-46 seconds. In the KESS region ARGOS satellite overpasses provided position fixes about once per hour. On average, the KESS profiling floats received about 7 position fixes during their 8.5 hours on the surface. The elapsed times between re-surfacing and the first position fix, and between the last position fix and subsequent diving, were each about 40 minutes.

During May–November, 2004, 687 T/S profiles and 4748 float position fixes were obtained. In the present analysis, we calculated dynamic heights from the T/S profiles. Velocities at the parking depth (see Fig. 4a) were evaluated from the float satellite position fixes by applying the method of Park et al. (2005): the float diving and re-surfacing locations are first estimated by extrapolating the satellite position fixes by using the linear and inertial velocity model; the parking depth velocities are then obtained by dividing the distance between the diving and re-surfacing locations by the time elapsed from the diving to the re-surfacing (the times are derived from float's metadata and the ARGOS messages). Notice that, if the velocity at the parking depth is 10 cm s^{-1}, the diving and re-surfacing locations could be about 43 km apart for a 5-day cycle. Thus the parking depth velocity is actually the averaged velocity of about 5 days in time and of tens kilometers along the float track at the parking depth. Despite this, in our analysis the parking depth velocities are assumed to be in the middle of the diving and re-surfacing locations/times.

There are two sources of error in the parking depth velocity estimates. One is associated with estimating either diving or re-surfacing locations by extrapolating satellite position fixes. On average, satellite position fixes become available for re-surfacing floats only after 42 minutes; for diving floats, the last satellite position occurs at an average of 37 minutes beforehand. This uncertainty can be assessed by withholding the last satellite position fix and using the remaining position fixes to extrapolate to it. In the present dataset, the distances between withheld position fixes and extrapolated ones have a median of 881 m.

The second error source is related to the velocity shear above the parking depth. The velocity shear is defined as $\vec{v}'(z) = \vec{v}(z) - \vec{v}_p$, where $\vec{v}(z)$ is the vertical velocity profile and $\vec{v}_p$ is the parking depth velocity. This error represents the extra float drift induced by $\vec{v}'(z)$ during float's ascending and descending motions. The ascent has a known duration (T_{ascent}) and an approximately constant ascent rate (w), so we are able to estimate the extra float drift during the ascent as

$$\int_0^{T_{ascent}} \vec{v}'(w \cdot t) dt, \tag{1}$$

where t is the time. The velocity shear $\vec{v}'(z)$ is assumed to follow the shape of the first baroclinic mode (in Section 4 we will show that the velocity shear profiles are indeed dominated by the first baroclinic mode), and is constructed by using the float surface velocities and the estimated parking depth velocities. The float surface velocities were produced when we estimated the diving and re-surfacing locations. In the present dataset, the median of the extra float drifts during ascent is 2,096 m. We can not make the same estimate for the descent, because the descent rate is unknown. The descent of the float may take twice as long as its ascent does, but the float sinks quickly in the upper layer and spends most of the time at the depths close to the parking depth. As argued by Park et al. (2005), one can thus take the uncertainty estimate for the ascent as an upper bound for the descent, or 2,096 m of additional float drift.

Therefore, in terms of the "drift", there are two sources of error in the parking depth velocities: 881 m in estimating either diving or re-surfacing locations and 2,096 m during either descending or ascending. Since they are uncorrelated, we have a total uncertainty of $\sqrt{2 \times 881^2 + 2 \times 2096^2} \approx$ 3215 m. Dividing by 111.5 hours, the average time that the floats stay below the sea surface in one cycle, the total "drift" uncertainty leads to an error estimate of 0.8 cm s^{-1} for the parking depth velocities. Notice that this error estimate is for the "instrumental" error. The "instrumental" error is introduced during the process of generating the velocity vectors (see Fig. 4a), which serve as a part of the starting dataset in this study. Given that the goal of this study is to describe the large-scale, mean state of the RG during May–November, 2004, mesoscale variability actually introduces an uncertainty (estimated later in the paper) larger than this "instrumental" error.

In addition to the KESS profiling float data, we used 14 full-depth CTD profiles taken in the RG during the KESS deployment cruise in May 2004 (see Fig. 3 for the locations). We also used the AVISO SSH anomaly dataset compiled by the CLS Space Oceanographic Division of Toulouse, France. The SSH anomaly dataset merges the TOPEX/Poseidon, Jason-1, and ERS-1/2 along-track SSH measurements, has a 7-day temporal resolution and a $1/3^\circ \times 1/3^\circ$ spatial resolution, and covers the period from October 1992 to December 2005.

3 Horizontal Velocities of the RG

As stated in the previous section, the KE/RG system was in a stable state from May 2004 to November 2004, when the KESS profiling float measurements were made. Compared with the climatology of the surface dynamic height in Fig. 1, the SSH from May–November 2004 shown in Fig. 3 indeed displays a swifter KE and a stronger RG. Notice that the elevation at the RG center, relative to its periphery, is less than 10 cm in the surface dynamic height climatology (Fig. 1) while it is about 50 cm in Fig. 3. This implies that from May–November 2004, the surface velocities in the RG are dominated by the temporal variations rather than by the climatology.

During May–November 2004, most of the 20 KESS profiling floats were trapped in the stable RG and revolved more than once; individual trajectories during this period of time can be found in Qiu et al. (2006). As shown in Fig. 4a, the velocity field at the parking depth (1,500 db) in the RG between 141° and 147°E is well sampled (314 vectors). Neighboring vectors might have been measured by different floats a few months apart, but an anticyclonic circulation is evident. The averaged major ellipse error of the gridded parking depth velocities is 3.7 cm s^{-1} (Fig. 4b), which is significantly larger than the "instrumental" error ($\sim$0.8 cm s^{-1}) estimated in the previous section, and it is likely due to mesoscale spatial and temporal variability.

Figures 4a, b show that the RG at the parking depth is centered approximately at (144°E, 34°N), and is narrower and swifter to the north than to the south, presumably because of its affinity to the eastward flowing KE jet. Fig. 4b also shows that variability, indicated by the standard error ellipses, is larger to the north. The RG is not exactly circular; as indicated by the 210 cm contour, its zonal extent is about 5 degrees longitude ($\sim$450 km) but the meridional extent is about 3 degrees latitude ($\sim$330 km).

The flow above the parking depth is approximately parallel to that at the parking depth. To demonstrate this, two-dimensional pressure fields at the parking depth and at three representative float sampling depths are compared in Fig. 5a, d, g. The pressure field at the parking depth

is estimated from the gridded parking depth velocities by using geostrophy, and those at the float sampling depths are estimated as follows. The geopotentials at each float sampling depth, referenced to the parking depth, are first calculated from available float T/S profiles in the RG, whose spatial coverage is similar to that of the parking depth velocities in Fig. 4a. These are then gridded in the same way as the parking depth velocities, except that the grids are offset by 0.25° in latitude/longitude. The pressure fields at the float sampling depths, such as those shown by the color shadings in Fig. 5a, d, g, are the sum of the geopotentials and the pressure field at the parking depth.

The geostrophic velocities are calculated using the pressure field data shown in the left-hand column of Fig. 5. These are then compared to the parking depth velocities, and the angle differences and magnitude ratios of the two velocities are given in the middle and right-hand columns of Fig. 5, respectively. The velocity magnitude ratio as a function of depth $\mathcal{R}$(z) is estimated by minimizing

$$\sum \left(|\vec{V}(z)| - \mathcal{R}(z) \cdot |\vec{V}_p| \right)^2,$$

where $|\vec{V}(z)|$ and $|\vec{V}_P|$ are the geostrophic velocities at depth z and the parking depth velocities, respectively, and the summation is over all data points at depth z. Since the angle differences in the middle column of Fig. 5 suggest that $|\vec{V}(z)|$ and $|\vec{V}_P|$ are parallel to each other when averaging over the RG, it makes sense to look at the velocity magnitude ratio.

The above calculations are repeated for all float sampling depths (Fig. 6). Averaging over the RG, the flow above the parking depth is approximately parallel to that at the parking depth (Fig. 6a). Furthermore, Fig. 6b shows that the RG strength increases monotonically from the parking depth to ∼500 db, and then remains approximately constant for the top 500 db. We will interpret this vertical structure in the next section by using dynamic modes. The RG at the surface is about three and a half times stronger than that at the parking depth. As shown in Fig. 5c, at the surface the RG circulates at a speed of ∼35 cm s^{-1} and at the parking depth its speed is ∼10 cm s^{-1}.

4 Mode Decomposition and Transport Estimate

To describe the vertical structure of the RG over the whole water column, we introduce dynamic modes. We will demonstrate that the vertical structure of the RG is dominated by the barotropic mode and the first baroclinic mode. The RG full-depth transport is derived from the barotropic mode; the depth averaged value of the baroclinic mode is zero and thus does not contribute to the net transport value.

4.1 Mode Decomposition

By using 14 full-depth CTD profiles acquired during the KESS deployment cruise in May 2004 (see Fig. 3 for their locations), we calculated dynamic modes (e.g. Chelton et al. 1998) and their averages, as shown in Fig 7a. Since the zero-crossing of the first baroclinic mode (∼1,345 db) was quite close to the float parking depth (1,500 db), the velocities at the parking depth only have minor contributions from the first baroclinic mode. If a velocity profile consisted only of the first baroclinic mode, and the surface velocity were 35 cm s^{-1}, then the velocity at the parking depth would be -1.7 cm s^{-1}.

We evaluated the relative importance of the baroclinic modes by using the 34 geostrophic shear profiles (their depth averages are zero) from the 34 neighboring pairs of the 14 full-depth CTD stations. The separation of the station pairs was 98 km on average, but ranged from 82 km to 112 km. For each geostrophic shear profile, baroclinic mode amplitudes $A_n (n = 1, 2, \cdots)$ were calculated. We define the depth-averaged variance of the shear profile $v(z)$ as $1/D \int_{-D}^{0} v^2(z) dz$, where D is the water depth. Since each baroclinic mode structure is normalized so that its depth-averaged, squared mode structure is unity, the depth-averaged variance of the shear profile is equal to $\sum_m A_m^2$. The relative explained variance of each baroclinic mode is then $\frac{A_n^2}{\sum_m A_m^2} \times 100\%$ $(n = 1, 2, \cdots)$. As shown in Fig. 7b, when averaged over the 34 geostrophic shear profiles, 86% of the total variance resides in the first baroclinic mode and 6% in the second baroclinic mode. Fig. 7c shows that when a geostrophic shear profile has significant variance in the second baroclinic mode,

it is quite weak. In this case the corresponding CTD station pair is likely to be either located near the center of the RG or aligned with the mainstream of the RG. In other words, the more energetic the geostrophic shear profile, the greater the variance in the first baroclinic mode.

From Fig. 7b, we conclude that the first baroclinic mode dominates the baroclinic component of the full-depth velocity profiles. Meanwhile, the previous direct velocity measurements (Firing 1998; Yoshikawa *et al.* 2004) have shown that the barotropic mode is significant in the RG. Given these observations, it is reasonable to assume that the barotropic and first baroclinic modes are the two most important modes. Under this assumption, the ratio profile $\mathcal{R}(z)$ in Fig. 6b is fitted by a model composed of the barotropic and first baroclinic modes using a least-squares approach. In other words, the following quantity is minimized:

$$\int_{-1500}^{0} (\mathcal{R}(z) - A_{bt}F_0(z) - A_{bc}F_1(z))^2 dz,$$

where $F_0(z)$ and $F_1(z)$ are the barotropic and first baroclinic mode structures shown in Fig 7a. The fitting procedure gives the amplitudes of the barotropic and first baroclinic modes as A_{bt}=1.08 and A_{bc}=0.93 (Fig. 8a), resulting in the mode amplitude ratio $A_{bc}/A_{bt} = 0.86 \pm 0.10$. The confidence interval is based on fitting the lower and upper bounds of $\mathcal{R}(z)$ (see Fig. 6b). Including the second and third baroclinic modes in the model does not alter our results significantly (by about 5% in terms of the mode amplitudes); the amplitudes come to 1.12, 0.89, 0.04, 0.01 for the barotropic and the first three baroclinic modes, respectively.

We thus use $A_{bc} = (0.86 \pm 0.10)A_{bt}$ to approximate the vertical structure of the RG as

$$F_{RG}(z) = F_0(z) + (0.86 \pm 0.10)F_1(z).$$

In Fig. 8a, the canonical vertical structure $F_{RG}(z)$ indicates that the RG flows in the same direction at all depths, from the surface to the bottom. In Fig. 8b, $F_{RG}(z)$ is also compared with two LADCP cross-track profiles in the southwestward flow region (see Fig. 2 for the locations of stations A and B). The fair agreement should be no surprise, since altimetry measurements have revealed that

the RG and the KE were both in the stable state during 1993 and 2004 (Qiu and Chen 2005). This agreement lends credibility to the inference of the vertical structure $F_{RG}(z)$, however, since the LADCP profiles are full-depth, direct observations.

Combining the vertical structure $F_{RG}(z)$ with the horizontal velocities from Fig. 4b, one can obtain an approximate view of the three-dimensional velocity field of the RG. The RG circulates in the same anticyclonic direction from the surface to the bottom. It has an anticyclonic surface velocity on the order of 35 cm s^{-1} and an anticyclonic bottom velocity on the order of 5 cm s^{-1}. In addition, the LADCP observations in Fig. 2 display additional features along the cruise track. One can see, as examples, an upward tilt of the RG towards the south, and extraordinary vertical variability between the southwestward and northeastward currents near 1,000 m.

4.2 Transport Estimate

As shown in Figs. 3 and 4a, the 34°N latitude and 144°E longitude lines cross near the center of the RG at the sea surface and at the parking depth. The transport of the RG is thus estimated by using the north-south component of the parking depth velocities within half a degree of latitude 34°N and by using the east-west component within half a degree of longitude 144°E (see Fig. 4a for the float parking depth velocities in those areas).

The parking depth velocities V_p^B are first binned within a 1/3° latitude or longitude band (Fig. 9a, b). Under the assumption that the binned velocities consist only of the barotropic and first baroclinic modes, each binned velocity is then expressed as follows:

$$V_p^B = 1 \cdot A_{bt}^B - 0.13 \cdot A_{bc}^B, \tag{2}$$

where the factors 1 and -0.13 are $F_0(z)$ and $F_1(z)$ evaluated at the parking depth, respectively (see Fig. 7a). Applying the mode amplitude ratio $A_{bc}^B/A_{bt}^B = 0.86$ from the previous subsection to Eq. 2 yields the barotropic mode amplitude (i.e., depth-averaged velocity)

$$A_{bt}^B = V_p^B/(1 - 0.86 \times 0.13). \tag{3}$$

The small value of $F_1(z)$ at the parking depth (0.13) indicates that the conversion from V_p^B to A_{bt}^B is not very sensitive to the mode amplitude ratio A_{bc}^B/A_{bt}^B; the parking depth velocities are dominated by the barotropic mode. The 10% uncertainty in the mode amplitude ratio A_{bc}^B/A_{bt}^B results in only a 1-2% uncertainty in A_{bt} and hence in the net transport. This is smaller than the uncertainty caused by variability in the parking depth velocities, which is estimated to be about 10%.

Accumulative transports are obtained by integrating A_{bt}^B from the east to west or from south to north, and multiplying by the mean depth of 5,160 m (Fig. 9a, b). The minimum of the accumulative transport shown in Fig. 9 is taken as the transport estimate for the RG. These values are 108.5±9.6 Sv along 34°N, and 92.8±7.2 Sv along 144°E. The error ranges given for the transport estimates stem from the standard errors of the binned velocities. By averaging the two estimates, the final transport estimate with one standard error is 101±8 Sv. Although the float velocities are independent at different locations, the two transport estimates may not be independent entirely. Recall that the two transport estimates have used the same conversion formula (Eq. 3), which are derived by using all parking depth velocities and T/S profiles in the RG together.

We can also infer the RG transport from the two-dimensional pressure field at the parking depth (see the white contours in Fig. 5a, where the maximum value of the pressure is 16 cm). Notice that we have used the geostrophy relationship in obtaining the pressure field at the parking depth (P_p in dynamic height cm). Under geostrophy, the streamfunction at the parking depth is gP_p/f, where g is the gravititational acceleration and f is the Coriolis parameter. Applying the same conversion used for the parking depth velocities (Eq. 3), we find the barotropic component of the streamfunction to be

$$\frac{gP_p}{f} \times \frac{1}{1 - 0.86 \times 0.13}.$$

The RG transport is

$$\frac{gH}{f}\Delta P_p \times \frac{1}{1-0.86\times 0.13},$$

where ΔP_p is the pressure difference in dynamic height between the RG's center and its periphery, and H is the mean depth of the RG (5,160 m). For $\Delta P_p = 14 \pm 2$ cm (the uncertainty reflects the difficulty in estimating the pressure at the periphery), the RG transport is 98±14 Sv, which is consistent with the results of Fig 9.

5 Summary and Discussion

During May–November, 2004, 20 profiling floats were deployed in the RG region south of the KE. As the KE and RG systems were in a stable state, most of these floats remained within the RG. We have limited our analysis to this period because the RG was strongly influenced by an intense, westward moving cyclonic eddy after November 2004. We have shown that the anticyclonic circulations of the RG at different depths in the upper 1,500 db are approximately parallel to each other, with the speed at the surface (35 cm s^{-1}) being about three and a half times larger than that at the parking depth (10 cm s^{-1}).

The full-depth vertical structure of the RG velocity field is dominated by the barotropic and first baroclinic modes. The two modes are of the same order of magnitude; the amplitude of the first baroclinic mode is about 0.86 times that of the barotropic mode. The two modes are combined in such a way that the resulting RG circulates anticyclonically at all depths, from the surface to the bottom. Its bottom velocity is on the order of 5 cm s^{-1}. The equivalent barotropic vertical structure is similar to that obtained by a full-depth LADCP observation in 1993, when the RG was also in the stable state.

From the (depth-averaged) barotropic component of the RG velocity field, the transport is estimated as 101±8 Sv (one standard error). Our transport estimate is comparable to that made in 1993 by the LADCP observation (∼86 Sv near 144.9°E, Firing 1998), but is significantly larger than those made in 2000 (∼50 Sv along 146°25′E) and in 2001 (∼34 Sv along 152°30′E) estimated

by Yoshikawa et al. (2004). Decade-long altimetric measurements revealed that the RG was in a stable state before 1995 and after 2002, and in an unstable state between 1995-2002 (Qiu and Chen 2005). The variations of the RG transport observed in 1993, 2000, 2001, and 2004 are consistent with the findings by Qiu and Chen (2005) that the RG during the stable state is about twice as strong as it is during the unstable state.

We have described the RG in the stable state by pooling all the float measurements during the period from May–November 2004, and averaging them azimuthally. Furthermore, we have noticed that the RG is swifter, narrower, and more variable to the north than to the south. This is no surprise, since the RG makes contact with the KE jet in the north. Exactly how this interaction takes place, however, can not be addressed by the present dataset and is a future KESS collaborative analysis objective.

The hypothesis that the first baroclinic mode dominates the baroclinic component of the velocity field is validated by the geostrophic shear profiles obtained by CTD stations with a spacing of ∼100 km. Our mode decomposition in Section 4 is applied only to the gyre-averaged ratio profile (Fig. 6b) and to the binned velocities (Fig. 9). Meanwhile, individual velocity measurements do have significant mesoscale variations as indicated by the standard error ellipses in Fig. 4b and by the scatter in the crosses of Fig. 9. The vertical structures of these mesoscale motions are unknown and are poorly resolved by our profiling float data.

The method to estimate the diving and re-surfacing locations used in Park et al. (2005) also produced float surface velocities, but we chose to use these velocities only to quantify the uncertainty in our parking depth velocities (Eq. 1). The float surface velocities have non-geostrophic components such as Ekman drift and windage effect, which are undesirable when inferring full-depth vertical structures in the RG.

As a part of the collaborative KESS program, the RG has also been observed by an array of CPIES (Current and Pressure recording, Inverted Echo Sounder) and moored current meters (see Fig. 1 in Qiu et al. 2006). In future analyses, it will be interesting to compare the RG structure

derived from the present study to that from the moored measurements data, which will provide time series information on the temporal variability of the KE and RG systems.

Acknowledgments

Comments made by the anonymous reviewers and Kathleen A. Donohue have significantly improved this study. The full-depth CTD profiles were collectively obtained as a part of Kuroshio Extension System Study (KESS) project. We thank other PIs (Kathleen A. Donohue, D. Randolph Watts, Humio Mitsudera, Nelson G. Hogg, and Steven Jayne) for their participation and effort. The merged T/P, Jason-1 and ERS-1/2 altimeter data is provided by the CLS Space Oceanography Division as a part of the Environment and Climate EU ENACT project. The support of the National Science Foundation through grant OCE-0220680 to UH, as a part of the collaborative research project KESS, is also gratefully acknowledged.

References

Chelton D. B., R. A. deSzoeke, and M. G. Schlax, 1998: Geographical variability of the first baroclinic Rossby radius of deformation. *J. Phys. Oceanogr.*, **28**, 433–460.

Firing, E., 1998: Lowered ADCP development and use in WOCE. *International WOCE Newsletter*, **30**, 10–14.

Niiler, P. P., N. A. Maximenko, G. G. Panteleev, T. Yamagata, and D. B. Olson, 2003: Near-surface dynamical structure of the Kuroshio Extension. *J. Geophys. Res.*, **108 (c6)**, 3193, doi:10.1029/2002JC001461.

——, Q. J. Schmitz, and D.-K. Lee, 1985: Geostrophic volume transport in high eddy-energy areas of the Kuroshio Extension and Gulf Stream. *J. Phys. Oceanogr.*, **15**, 825–843.

Park, J. J., K. Kim, B. A. King, and S. C. Riser, 2005: An advanced method to estimate deep currents form profiling floats. *J. Atmos. Oceanic Techol.*, **22**, 1,294–1,304.

Qiu, B., 2003: Kuroshio Extension variability and forcing of the Pacific decadal oscillations: Responses and potential feedback. *J. Phys. Oceanogr.*, **33**, 2,465–2,482.

——, and S. Chen, 2005: Variability of the Kuroshio Extension jet, recirculation gyre and mesoscale eddies on decadal timescales. *J. Phys. Oceanogr.*, **35**, 2,090–2,103.

——, P. Hacker, S. Chen, K. A. Donohue, D. R. Watts, H. Mitsudera, N. G. Hogg, and S. R. Jayne, 2006: Observations of the subtropical mode water evolution from the Kuroshio Extension System Study. *J. Phys. Oceanogr.*, **36**, 457–473.

Schmitz, W. J., P. P. Niller, R. L. Bernstein, and W. R. Holland, 1982: Recent long-term moored instrument observations in the Western North Pacific. *J. Geophys. Res.*, **87**, 9,425 – 9,440.

Teague, W.J., M.J. Carron, and P.J. Hogan, 1990: A comparison between the Generalized Digital Environmental Model and Levitus climatologies. *J. Geophys. Res.*, **95**, 7167–7183.

Wijffels, S.E., M.M. Hall, T.M. Joyce, D.J. Torres, P. Hacker, and E. Firing, 1998: Multiple deep gyres of the western North Pacific: A WOCE section along 149°E. *J. Geophys. Res.*, **103**, 12,985–13,009.

Yoshikawa, Y., J. A. Church, H. Uchida, and N. J. White,, 2004: Near bottom currents and their relation to the transport in the Kuroshio Extention. *Geophys. Res. Lett.*, **31**, L16309, doi:1029/2004GL020068.

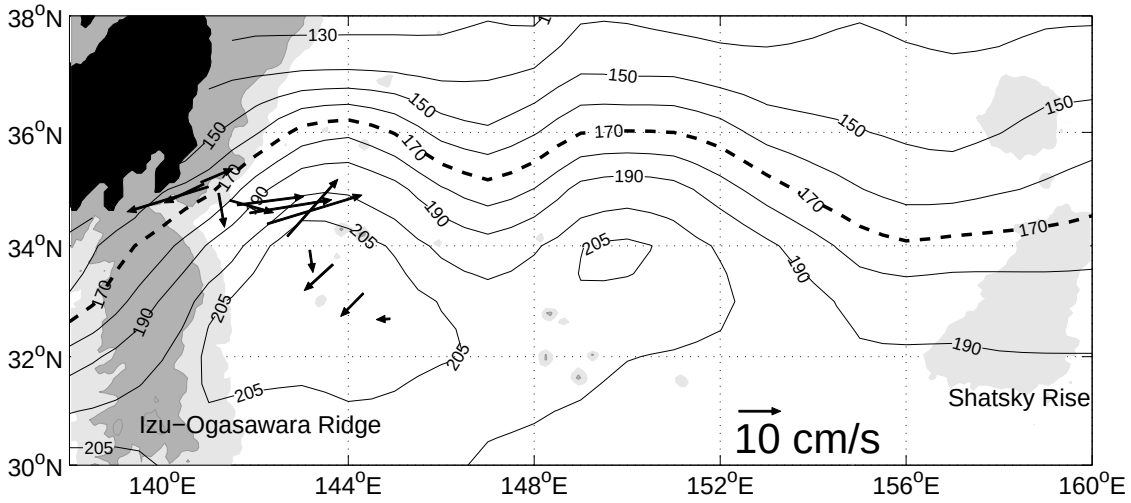

Figure 1: Mean sea surface dynamic height in cm relative to 1,000 db, from Teague et al. (1990). The contour interval is 10 cm. A 205 cm contour is added to signify the recirculation gyre south of the Kuroshio Extension. Arrows indicate the depth-averaged LADCP velocities along the WOCE P10 line in November 1993 (Firing 1998); a full-depth view of the LADCP cross-track velocities is given in Fig. 2. Light and dark gray shadings denote water depths of 2,000 m and 4,000 m, respectively.

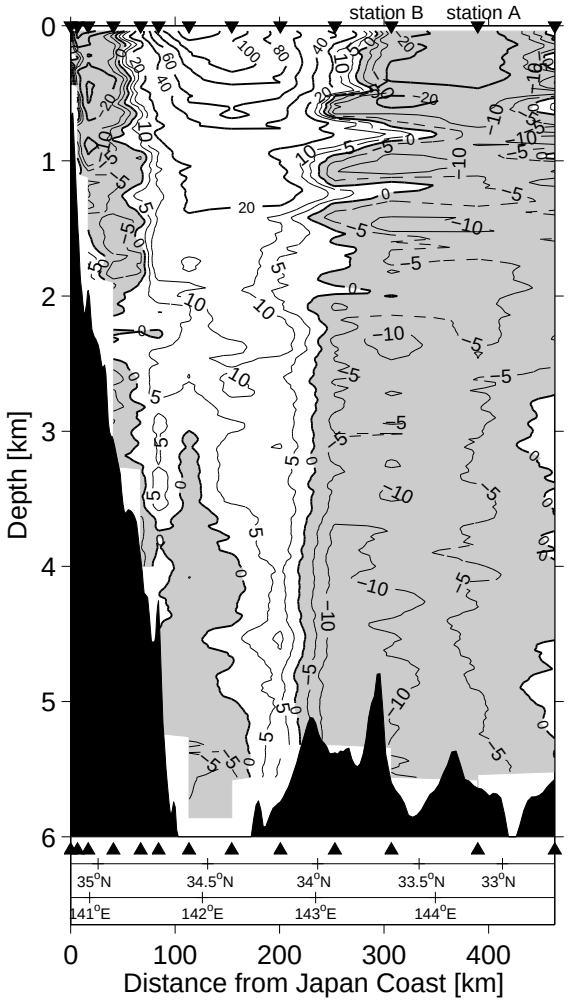

Figure 2: Cross-track LADCP velocities along the WOCE P10 line in November 1993, as a function of distance to the southeast from the Japan coast (see Fig. 1 for LADCP station locations and the depth-averaged LADCP velocities). The LADCP profile locations are indicated by the solid triangles. The vertical profiles at stations A and B are shown in Fig. 8b. Longitudes and latitudes along the cruise track are also indicated. The negative southwestward flow is shaded. The interval for thick contours is 20 cm s^{-1}, and thin contours are added in between at ± 5 and ± 10 cm s^{-1}.

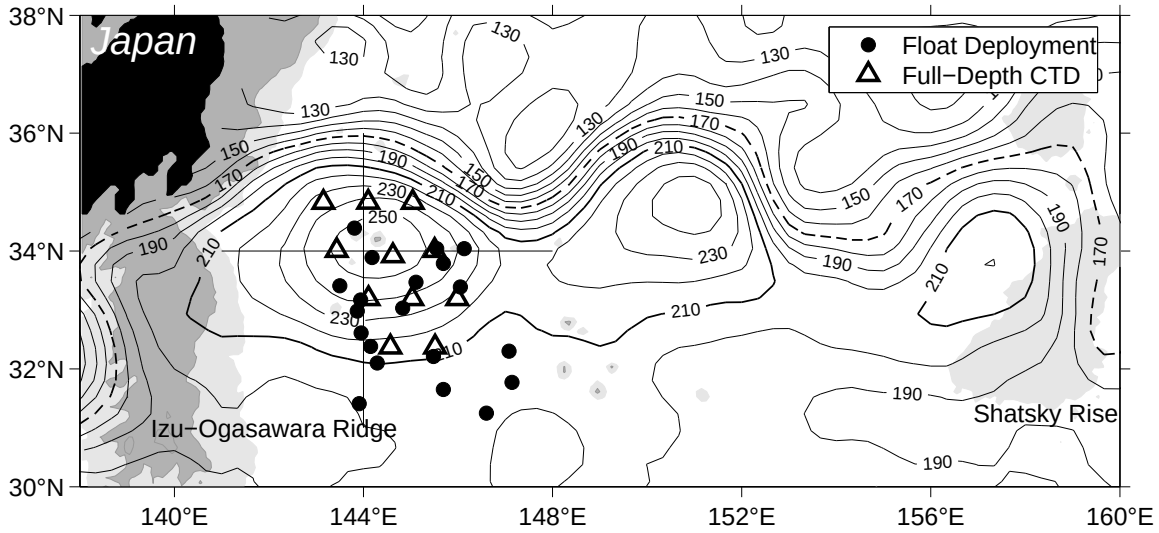

Figure 3: Sea surface height in cm, taken as the sum of the altimetric SSH anomaly, averaged over the period from May–November 2004, and the Teague et al. (1990) sea surface dynamic height. Solid dots are the deployment locations of the 20 KESS Apex floats. Black triangles are the 14 full-depth CTD stations, some of which near the center of the RG are duplicated in space but separated in time by more than 10 days. Light and dark gray shadings denote water depths of 2,000 m and 4,000 m, respectively. The two lines are along 34°N and 144°E, respectively.

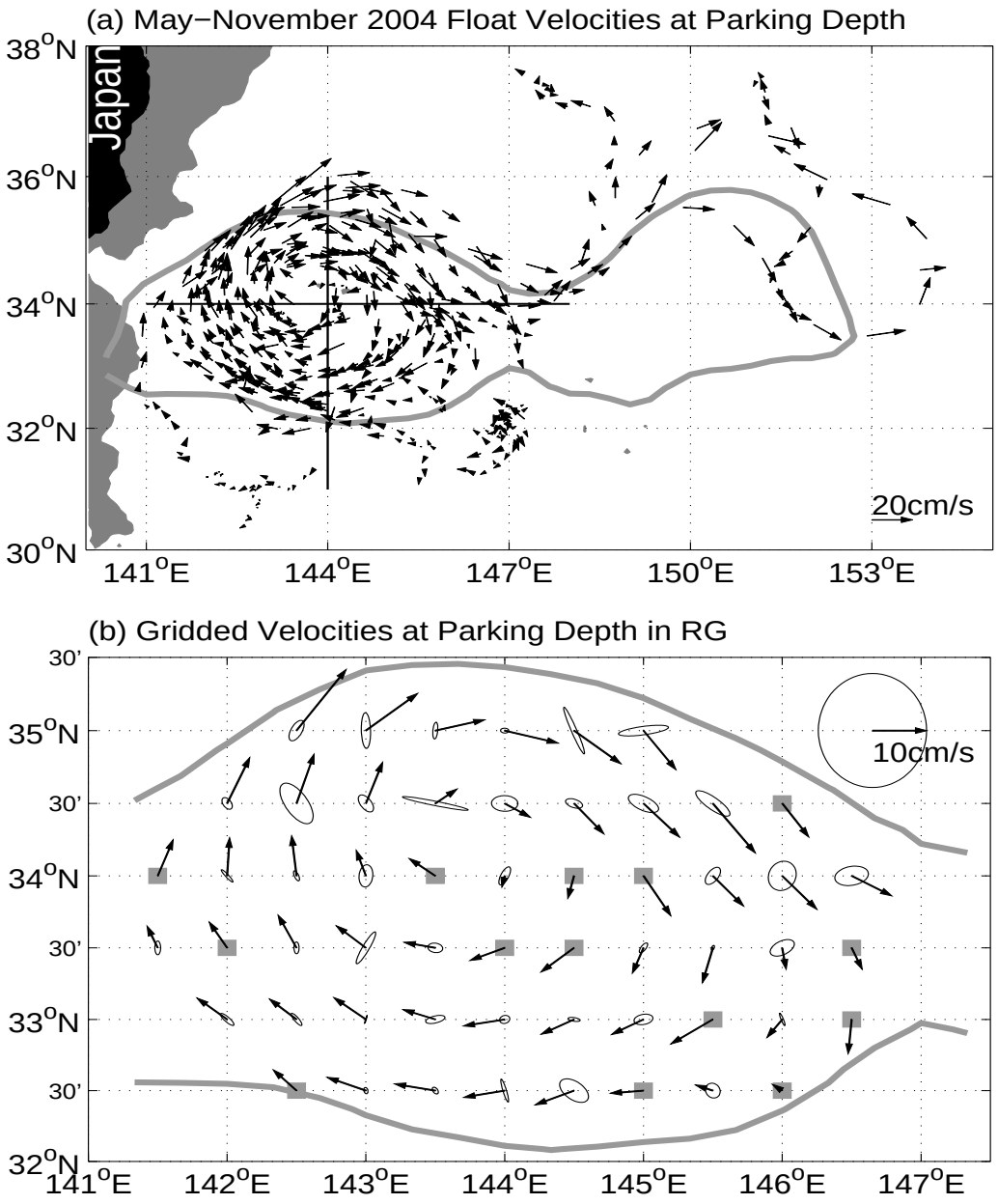

Figure 4: (a) Float velocities at the parking depth. The vectors start from the middle of the diving and re-surfacing locations. The gray shading indicates water depth < 2000 m. (b) Gridded velocities at the parking depth. Standard error ellipses are shown if there are 3 or more float velocities within 25 km of the grid points; otherwise, gray squares are added. In both panels, the thick gray line is the 210 cm SSH contour from Fig. 3, indicating the RG boundary.

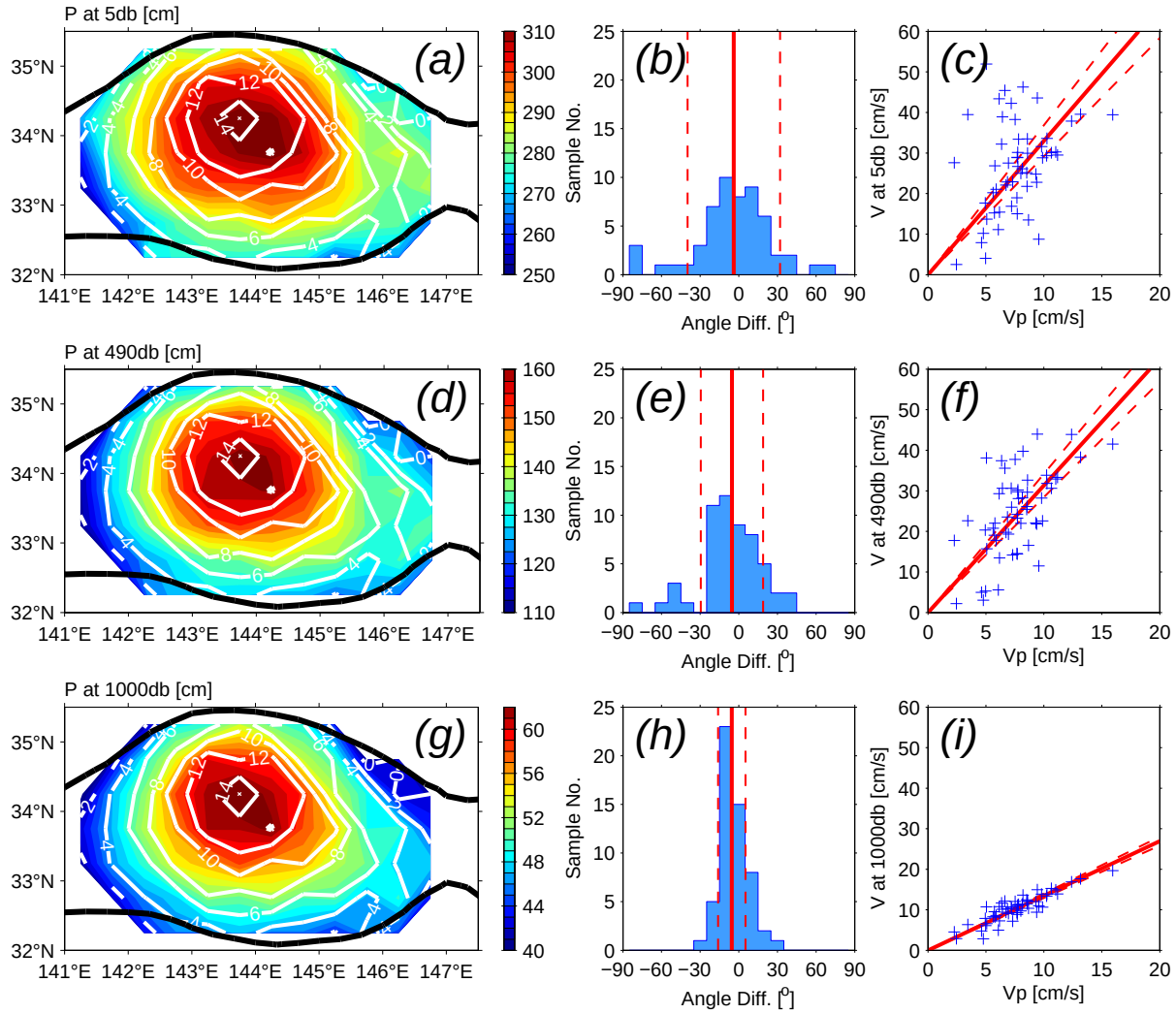

Figure 5: (a) Pressure fields at 5 db (color shading) and at the parking depth (1500 db, white contours). Both are in units of dynamic height cm. The thick dark lines are the 210 cm SSH contours from Fig. 3, indicating the RG boundary. (b) Histogram of the angle differences between the geostrophic velocities at 5 db and the gridded parking depth velocities V_p (shown in Fig. 4b). A negative angle means that the velocity at 5 db is more clockwise than that at the parking depth. The solid and dashed red lines indicate the median value and standard deviation. (c) Scatter plot of the geostrophic velocities at 5 db vs. V_p. The solid and dashed red lines indicate the best-fit lines and their 95% confidence invervals; the slopes of these lines give the ratio between the two velocities. Panels (d,e,f) and (h,g,i) are the same as Panels (a,b,c), but at depths of 490 db and 1,000 db, respectively.

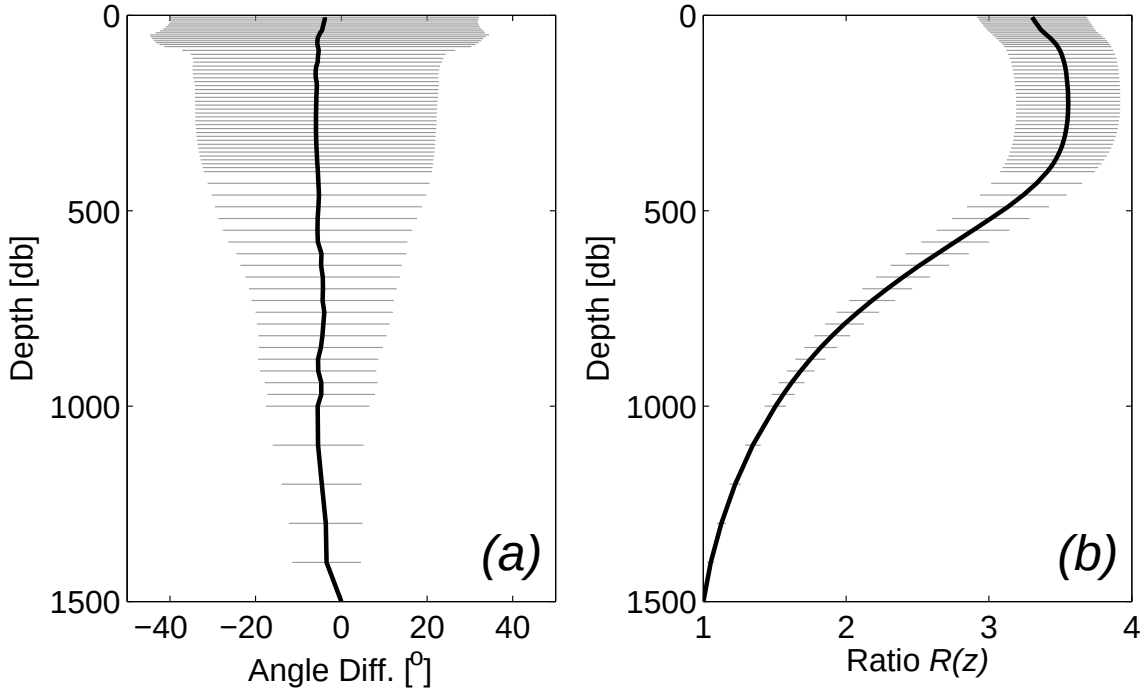

Figure 6: (a) Medians (dark line) and standard deviations (gray lines) of the angle differences between the geostrophic velocities at each float sampling depth and the gridded parking depth velocities V_p. Those at depths of 5 db, 490 db, and 1000 db have already been shown in the middle column of Fig. 5 as red lines. (b) The ratio of the geostrophic velocities at each float sampling depth to V_p. The ratios at depths of 5 db, 490 db, and 1000 db are also shown as red lines in the right-hand column of Fig. 5. The 95% confidence levels are indicated by the gray lines.

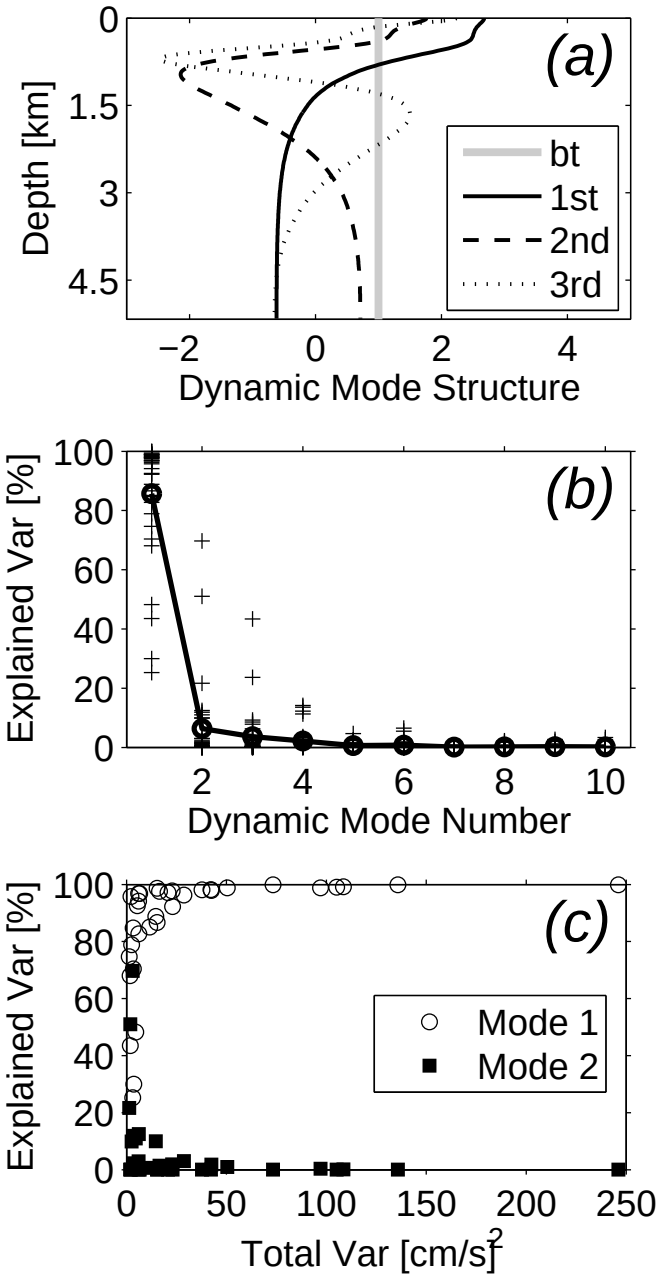

Figure 7: (a) Vertical structures of the barotropic ("bt") mode and the first three baroclinic dynamic modes in the RG. The modes have been normalized such that their depth-averaged, squared vertical structures are unity. (b) The proportion of variance contributed by each dynamic baroclinic mode, for each of the 34 geostrophic shear profiles (crosses). The solid line with circles is the average of each mode. (c) Relative variance contributions of the first and second modes, as function of the total variance in the geostrophic shear profiles.

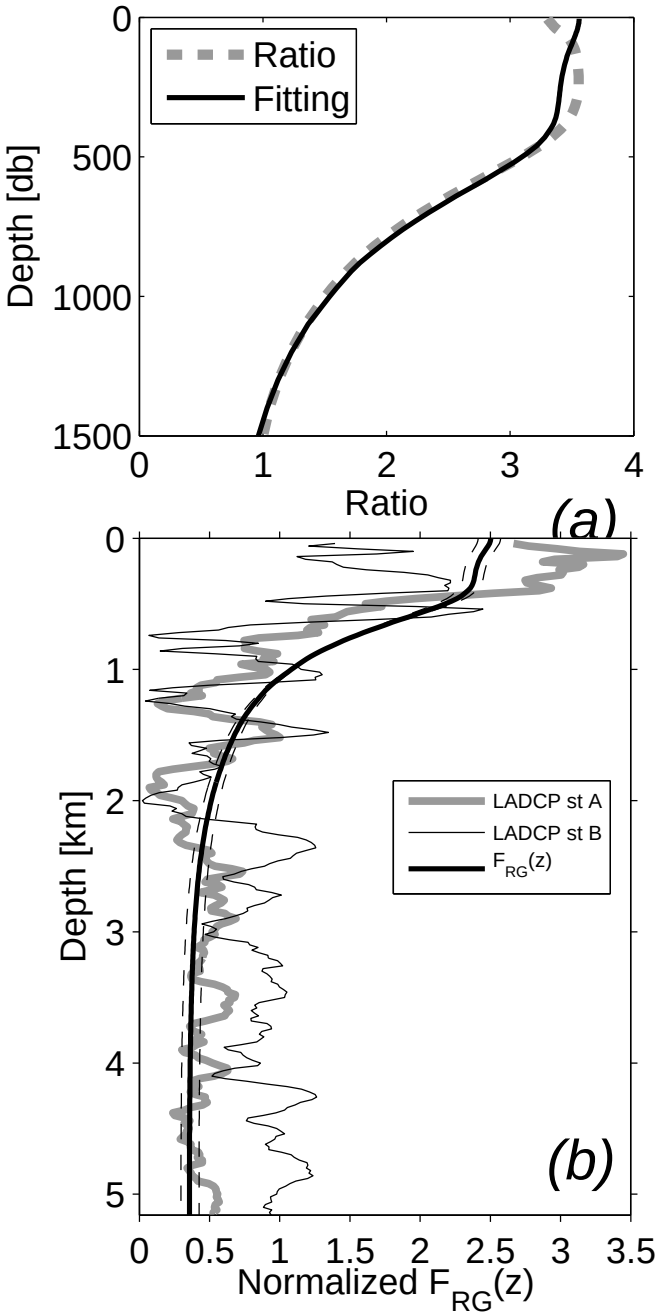

Figure 8: (a) The ratio shown in Fig. 6b (dashed line) is fitted by a linear combination of the barotropic and first baroclinic modes (solid line). (b) The vertical structure $F_{RG}(z)$, normalized so that the depth-averaged, squared $F_{RG}(z)$ is unity. The dashed lines indicate the range obtained by varying the mode amplitude ratio within its 95% confidence interval. The LADCP vertical profiles are the same cross-track velocities as those indicated in Fig. 2 at stations A and B, except that they are normalized in the same manner as $F_{RG}(z)$.

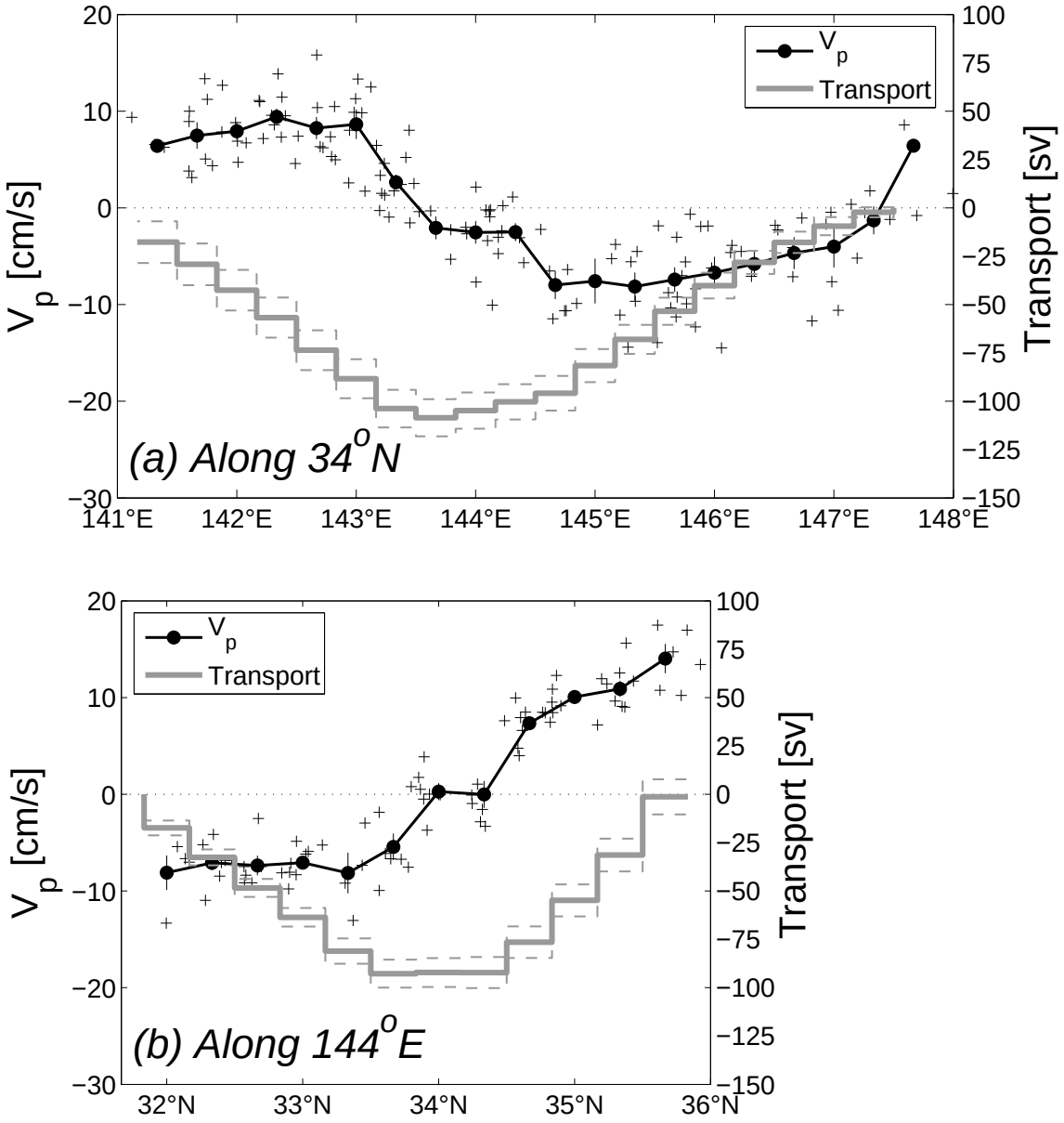

Figure 9: (a) North-south components of the parking depth velocities (crosses) within half a degree of latitude 34°N. The line with circles and error bars shows the bin-averages and standard errors over each 1/3° longitude bin. The gray solid and dashed lines are the derived accumulative transport and standard error range from 147.5°E. The scale on the left is for the velocity and on the right for the transport. (b) as above, but for east-west components of the parking depth velocities (crosses) within half a degree of longitude 144°E. The accumulative transport starts from the southern end.